SUPPLEMENTARY INFORMATION

Why copper is preferred over iron for oxygen activation and reduction in heme-copper oxidases

Ambika Bhagi-Damodaran,[†] Matthew A. Michael,[‡] Qianhong Zhu,[#] Julian Reed,[§] Braddock A. Sandoval,[†] Saumen Chakraborty,[†] Evan Mirts,[‖] Pierre Moënne-Loccoz,[#,*] Yong Zhang,[‡,*] Yi Lu[†,§,‖,*]

[†]Department of Chemistry, [§]Department of Biochemistry, [‖]Center for Biophysics and Quantitative Biology, University of Illinois at Urbana-Champaign, Urbana, IL, USA. [‡]Department of Biomedical Engineering, Chemistry, and Biological Sciences, Stevens Institute of Technology, Hoboken, NJ, USA. [#]Division of Environmental & Biomolecular Systems, Institute of Environmental Health, Oregon Health & Science University, 3181 SW Sam Jackson Park Road, Portland, OR, USA.

*Corresponding author emails: yi-lu@illinois.edu; yong.zhang@stevens.edu; moennelo@ohsu.edu.

Table of Contents:

Supplementary methods:

All chemicals, unless otherwise specified, were obtained from Sigma (St. Louis, MO) or Fisher Scientific (Hampton, NH).

Purification of proteins

Fe_BMb was expressed and purified as reported previously.[1] Briefly, apo-protein was expressed and localized to the inclusion bodies of BL21(DE3) cells. The cells were then lysed by sonication and denatured with 6 M guanidine chloride. Heme *b* was added to the denatured cell solution, which was then dialyzed against 10 mM TRIS-H_2SO_4 pH 8 at least 4 times. The resulting protein solution was concentrated by Amicon with a 10,000 MWCO filter, and passed through a size exclusion column to achieve homogeneity. Protein fractions with r/z value greater than 4 were then combined and chelexed to remove any metal ions at the Fe_B site as per a procedure reported previously.[2,3] Final yield of the protein was ~ 40 mg/L. WTMb was expressed and purified as reported previously[4] and its yield was typically ~100 mg/L.

Characterization of Fe_BMb variants *via* UV-Vis spectroscopy

UV-vis data were collected on a Hewlett-Packard 8453 and CARY 5E spectrophotometer. Table S1 enlists the spectral features of oxidized and reduced forms of Fe_BMb and WTMb variants utilized in this work. The oxidized form of the proteins show a Soret band at 400 nm range followed by α and β bands in the visible region, typical of a well-folded met-myoglobin.[5] Extinction coefficient of the proteins was determined by hemochromogen assay where the wavelength maximum (in nm) and extinction coefficient used for the α peak of heme *b* was 556 and 36.5 mM^{-1} cm^{-1} respectively.

Metal titration and analysis

The Zn^{II} and Fe^{II} bound Fe_BMb variants were prepared as described previously with slight modifications.[6] Briefly, E-Fe_BMb(Fe^{III}) was degassed and transferred in anaerobic glovebag, where they were reduced using dithionite and exchanged with a PD10 column

equilibrated with 50 mM Bis-TRIS buffer at pH 7.3. To obtain Zn^{II} and Fe^{II}-bound Fe_BMb variants, 1 molar equivalent (with respect to protein) each of $ZnCl_2$ and $FeCl_2$ solution was added to E-$Fe_BMb(Fe^{II})$ respectively. To obtain Cu^{I}-$Fe_BMb(Fe^{II})$, 3 equivalent of tetrakis(acetonitrile)Cu(I)hexafluorophosphate dissolved in acetonitrile was added to E-Fe_BMb and any unbound Cu(I) ions were removed by a PD10 column equilibrated with 50 mM Bis-TRIS buffer at pH 7.3. Bathocuproine was used to determine the amount of Cu^{I} bound to Fe_BMb. An extinction coefficient of 13,800 M^{-1} cm^{-1} at 480 nm was used for the Cu^{I}-bathocuproine complex, as per which 3 equivalents of Cu^{I} bound to each equivalent of Fe_BMb. When 3 molar equivalent of Cu(I) was added to WTMb and run through PD-10 column, the bathocuproine assay showed that only 2 equivalents of Cu^{I} was bound to WTMb suggesting that the third equivalent of Cu(I) binds to the Fe_B center in Cu^{I}-Fe_BMb. The binding of the metal ion at the nonheme center of Fe_BMb was confirmed by bathochromic shifts in the UV-Vis spectra as can be seen in Figs. 1d and S2.

Oxygen consumption assay using an oxygen electrode

The rate of water and ROS production was measured and calculated as reported previously with slight modifications as described here.[1,7] The oxygen consumption assay was initiated by the addition of 18 μM of metal-bound Fe_BMb to 18 mM ascorbate and 1.8 mM of TMPD incubated in air saturated 100 mM phosphate buffer at pH 6. To calculate the percentage of ROS formation, we repeated the measurement of O_2 reduction in the presence of catalase (7 μM) and superoxide dismutase (SOD, 250 units), which selectively react with H_2O_2 and O_2^{2-} to produce O_2. By comparing the rates of reduction in the absence of and in the presence of catalase/SOD, the portion of O_2 reduction that is due to H_2O formation can be calculated, using a protocol reported previously. For experiments with Cu^{I}-$Fe_BMb(Fe^{II})$ in particular, we found that catalase removed the Cu^{I} ions from the Fe_B center and decreased the rates significantly. To avoid that, the Cu^{I} binding sites in catalase were saturated by adding 24 equivalents of Cu^{I} in the glovebag prior to the assay. The Cu^{I} bound catalase was checked for its activity by performing assays with H_2O_2 in the oxygen electrode before using it for the determination of H_2O_2 produced in experiments with Cu^{I}-Fe_BMb. The control experiments for WTMb (shown in

Fig. S4) were performed with 18 μM deoxy-WTMb mixed with 1 molar equivalent of Zn(II), Fe(II) and 3 molar equivalents of Cu(I) respectively. Fig. S9 shows how addition of increasing molar equivalents of Fe^{II} and Cu^{I} to $Fe_BMb(Fe^{II})$ impacted the total oxygen reduction rates. All assays were repeated at least six-times and error bars in the figures indicate standard deviation.

EPR sample preparation and data collection

All EPR samples were prepared in the presence of 10% glycerol in 50 mM Bis-TRIS pH 6.3 buffer. Rapid freeze-quench was used to prepare 50 ms and 100 ms. Cu^{I}-$Fe_BMb(Fe^{II})$ was prepared as described above and transferred into a syringe and sealed inside glove bag. The syringe was transferred outside for rapid freeze-quench. The O_2 saturated solution was transferred into another syringe. Rapid freeze-quench was performed at 25 °C, using an Update Instruments System 1000 equipped with a Wiskind Grid Mixer, a spraying nozzle, and a stirred isopentane bath, cooled by liquid nitrogen to approximately -130 °C. Cu^{I}-$Fe_BMb(Fe^{II})$ and O_2 saturated buffer (containing 10% glycerol each) were mixed and passed through a delay hose of appropriate length to give the desired quench time (50 ms and 100 ms). The sample was frozen by spraying into approximately -130 °C spectrophotometric grade isopentane in a Pyrex collection funnel attached to the EPR tube. A pre-cooled packing rod and syringe were used to pack the frozen powder to the bottom of EPR tube, while the whole set-up was kept in isopentane bath. The ~5s sample was prepared by manually mixing Cu^{I}-$Fe_BMb(Fe^{II})$ and O_2 saturated buffer followed by transferring and freezing the mixture in an EPR tube. The EPR samples were stored in liquid nitrogen for less than two days before data were collected.

X-band EPR spectra were collected on a Varian E-122 spectrometer at the Illinois EPR Research Center (IERC). The samples were collected at 30 K using liquid He, 5 mW power, and 9.05 GHz. Magnetic fields were calibrated with a Varian NMR gaussmeter, and the frequencies were measured with an EIP frequency counter.

XANES sample preparation and data collection

All XANES samples were prepared in the presence of 10% glycerol in 50 mM Bis-TRIS pH 6.3 buffer in a 30 mm cell sealed with Kapton film. Fe^{II}-$Fe_BMb(Fe^{II})$ was prepared as

described above and concentrated to ~1.6 mM. The 0s sample was prepared by freezing ~100 μL of Fe^{II}-$Fe_BMb(Fe^{II})$ in the XANES cell under anaerobic conditions. For the 60s sample, ~100 μL of Fe^{II}-$Fe_BMb(Fe^{II})$ solution was reacted with excess oxygen for 60s before freezing, and for the control sample, ~100 μL of 1.4 mM E-$Fe_BMb(Fe^{III})$ was mixed with 1 equivalent of Fe^{II} anaerobically, transferred to the XANES cell and frozen in liquid nitrogen. Fe-edge (7.112 keV) XANES were collected at the Stanford Synchrotron Radiation Lightsource (SSRL) operating at 3 GeV with currents ~500 mA on beamline 9-3 using a Si 220 monochromator ($\phi = 90°$, energy cutoff 12 keV) and a Rh-coated mirror. Data were collected in fluorescence mode on a Canberra 100-element Ge array detector with maximum count rates below 120 kHz. Soller slits and a 3 micron Z-1 (Mn oxide) filter were placed between the samples and the detector array to reduce Compton and elastic scattering. Edge energy was calibrated against a Fe reference foil that was scanned simultaneously with every sample. Samples were scanned 4-6 times divided between 2-3 spots (2 mm x 3 mm) in the sample holder at a temperature of 8-10 K and averaged for analysis. XANES data were collected from ~150 eV below and above the Fe-edge to assist in background subtraction and normalization with energy steps of 0.25 eV in the edge region. Data analysis was performed using Athena from the Demeter software suite. A flat pre-edge was achieved by subtracting a line anchored through points at least 30 eV below the edge, and the spectra were normalized by subtracting a second order polynomial fixed to points greater than 60 eV above the edge.

Spectroelectrochemical Measurements

The heme reduction potential (E°') was measured by a spectroelectrochemical method using an optically transparent thin-layer cell and the analysis of the data was performed as described previously.[4] The experiments were repeated at least twice and error in the E°' values indicate standard deviation.

Cyclic Voltammetry Measurements on Cu^{I}- and Fe^{II}- incorporated $Fe_BMb(Zn^{II})$

The Zn protoporphyrin IX incorporated Fe_BMb, called $Fe_BMb(Zn^{II})$, was prepared and characterized as described previously.[8] The Fe^{II} and Cu^{I} metal ions were incorporated at the Fe_B center of E-Fe_BMb in a similar manner as described for Fe_BMb. The addition of

metal ions caused a shift in the bands of UV-Vis spectra of $Fe_BMb(Zn^{II})$ as shown in Fig. S6. The resulting protein was subjected to a PD-10 column equilibrated in 50 mM Bis-TRIS pH 7.3 to remove any excess/unassociated metal ions. The reduction potential (E°) of the nonheme metal in $Fe_BMb(Zn^{II})$ was measured by cyclic voltammetry experiments. About 20 μL of 0.8 mM of Cu^{I}- and Fe^{II}- incorporated $Fe_BMb(Zn^{II})$ variants were drop-cast and let dry onto pyrolytic graphite electrodes and subjected to a potential sweep from -200 mV to 800 mV v/s Ag/AgCl electrode in 50 mM phosphate buffer at pH6 containing 100 mM $NaNO_3$. Fig. S10 shows the cyclic voltammogram obtained from these measurements. The experiments were repeated at least twice and error in the E°' values indicate standard deviation.

Stopped-flow UV-Vis kinetic measurements

Experiments were performed on an Applied Photophysics Ltd. (Leatherhead, U.K.) SX18.MV stopped-flow spectrometer equipped with a 256 element photodiode array detector. Two-syringe mixing was employed to mix equal volumes of Fe_BMb variants with volumetrically prepared oxygen saturated solutions. All reported data sets originally consisted of 200 spectra collected over 30 s using logarithmic sampling. The integration period and minimum sampling period were both 1 ms. A water bath, connected to the syringe compartment and set to 4ºC, provided temperature control. The actual temperature in the syringe compartment was measured to be ~ 8ºC. The instrument was prepared for anaerobic stopped-flow by rinsing its lines out several times with buffer that had been degassed by bubbling argon gas through it. Special glass outer syringes fit with Teflon stoppers into which an argon line was run maintained an oxygen free environment. The protein was degassed and prepared in an anaerobic glovebag as described before. To prepare oxygen saturated solutions, the buffer was degassed on the Schlenk line followed by bubbling with oxygen gas for 20 min in containers with only a small opening, to allow gases to escape.

Resonance Raman (RR) sample preparation and data collection on Fe_BMb variants

Attempt to prepare O_2-complex with E-$Fe_BMb(Fe^{II})$ and Zn^{II}-$Fe_BMb(Fe^{II})$ through manual mixing of the reduced proteins with O_2 saturated buffer led to poor enrichment in the oxy

complex and contamination with auto-oxidized protein. In contrast, rapid-freeze quench (RFQ) samples with a few milliseconds to 2 second freezing time showed highly reproducible accumulation of the oxy complexes (Fig. S11). Detailed procedure for the preparation of RFQ samples have been described previously.[9] Solutions of Fe_BMbs at 0.6 mM in 50 mM Bis-TRIS, pH 7.0, were loaded in RFQ glass syringes inside an anaerobic glovebox (Omnilab System,. Vacuum Atmospheres Co.). O_2 saturated buffer solutions were prepared by injecting 7 mL of $^{16}O_2$ or $^{18}O_2$ gas in 10-mL serum bottles containing 2.5 mL of degassed buffer and loaded in RFQ syringes after ~1 h incubation. Two syringes were mounted to the System 1000 Chemical/Freeze Quench Apparatus (Update Instruments) and immersed in a water bath at 4 °C. Reaction times were controlled by adjusting the displacement rate and the length of the reactor. For RFQ time points in the millisecond scale, a total of 250 µL of mixed solution was sprayed from the exit nozzle to a glass funnel connected with NMR tubes and filled with liquid ethane at -120 °C. Samples with reaction time on the second scale were injected directly inside the NMR tube before rapid freezing in liquid ethane. RR spectra were collected before and after removal of the cryosolvent by incubating the sample at -80°C for 2 hours. The RR spectra were obtained with a 407 nm excitation from a Kr laser (Innova 302C, Coherent) using a custom McPherson 2061/207 spectrograph equipped with a liquid-nitrogen cooled CCD detector (LN-1100PB, Princeton Instruments). A long-pass filter (RazorEdge, Semrock) was used to attenuate Rayleigh scattering. Measurements were performed in a backscattering geometry with the samples maintained at 110 K inside a liquid N_2 cooled sample holder and with the laser focused on the sample with a cylindrical lens. The high-frequency region of the RR spectra where fully symmetric porphyrin skeletal modes dominate was used to evaluate the accumulation of oxy-complex relative to deoxy- and met- forms. The deoxy-form is the hemeFe^{II} form and the met-form is the hemeFe^{III} form. Specifically, the major ν_4 mode occurs at 1353, 1376, and 1369 cm^{-1} in the deoxy, oxy, and met forms, respectively (see Fig. S11). The photosensitivity of each sample was evaluated by collecting short spectral acquisition with low laser power and spinning the NMR tube and comparing the porphyrin skeletal modes in the high-frequency region. While E-Fe_BMb(Fe^{II})-O_2 showed no significant photosensitivity, sample spinning was

required for Zn^{II}-Fe_BMb(Fe^{II})-O_2. The frequencies were calibrated relative to aspirin and are accurate to ±1 cm^{-1}.

Computational studies on Fe_BMb variants

A number of O_2 bound HCO models including E-Fe_BMb using the DFT method B3LYP with 6-311G* for all heavy atoms and 6-31G* for hydrogens, which is similar to the ones reported previously for heme and non-heme and copper protein model studies.[10-12] The initial structural models were built from the following X-ray structures with PDB files 3M38, 3M3B, 3M39, and 3M3A respectively. All first coordination shell residues are included in the models and the residues are truncated to Cα positions. The heme substituents were replaced with hydrogens. The labile water ligand in the original X-ray structures of Fe-Fe_BMb and Cu-Fe_BMb were allowed to be displaced by the incoming O_2 ligand. All models were subject to partial geometry optimizations with only protein residue Cα atoms fixed at the X-ray structure positions to mimic the protein environment, based on the previous work.[13] In the initial setup for Zn-Fe_BMb-O_2, heme iron and O_2 moiety are of Fe^{III}(S=1/2) anti-ferromagnetically coupled with O_2^- (S=-1/2) as reported recently.[14] In case where the second metal is Fe and Cu, the initial set up of non-heme site metal is in its oxidized state (i.e. Fe^{III} and Cu^{II}) with O_2 being set up as peroxide. In addition, both ferromagnetic and antiferromagnetic coupling modes between this site and heme iron were studied, as indicated by F or AF after the above respective model names. In addition to the electronic energy (E), the zero-point energy corrected electronic energy (E_{ZPE}), and the enthalpy and Gibbs free energies at the ambient conditions were also calculated in each case. All calculations were performed using the Gaussian 09 program.[15]

The optimized molecular structures of Zn^{II}-Fe_BMb(Fe^{III})-O_2^-, Fe^{III}-Fe_BMb(Fe^{III})-O_2^{2-} ,and Cu(II)-Fe_BMb-O_2^{2-} are shown in Fig. 4. The corresponding geometric parameters and charge and spin densities are listed in Table S2. The spin density of heme iron (ρ_{Fe}) in all models clearly indicates that it is oxidized to the ferric state (S=1/2), with the electron transferred to O_2 to activate it, since more electron populated into the frontier anti-bonding orbital of O_2 increases the bond length to help break it. For Zn-Fe_BMb-O_2, although Zn is coordinated with O, the bond is long, 2.340 Å. The spin density of the second metal (ρ_M) shows that Zn is redox-inert, and the heme iron-O_2 group is best described as Fe^{III}(S=1/2)

anti-ferromagnetically coupled with O^{2-} (S=-1/2), similar to those seen with single heme O_2 complexes. When the second metal becomes the redox-active iron, as seen from Table S2, spin density data (ρ_M=4.0 e) show that the non-heme iron is in-between Fe^{II} (S=2, with ρ~3.8 e) and Fe^{III}(S=5/2 with ρ~4.2 e).[16] The similar properties observed for both ferromagnetic and anti-ferromagnetic coupling modes suggest that these two couplings may be of similar energies, which is indeed the case as shown by energetic data in Table S3. Therefore, the anti-ferromagnetic coupling mode was chosen to further evaluate the most favorable spin state for the non-heme iron. As shown in Table S4, other spin states (S=3/2 and 1/2) have ~5 and ~20 kcal/mol higher energies, respectively. So, the sextet is most favorable. In the case of Cu as the second metal which is also the metal in HCO, much elongated OO bonds by ~0.10-0.12 Å compared to the Fe-Fe_BMb-O_2 were found. These results clearly indicate Cu is superior than other metals studied here to activate O_2, with the most lengthened OO bond length, which is also accompanied by shortest M-O bond length and concomitantly most shortened Fe-O bond length. The latter shows that Cu not only activates O_2 by donating its electron to O_2 with Cu being oxidized to Cu^{II} (its spin density is consistent with those reported in other Cu^{II} systems[17]), but also synergistically increased heme iron's activation on O_2 potentially through $d\pi$-$p\pi$ backbonding. As a matter of fact, O_2 (Q_{O2} in Table S2) charges has an excellent correlation with OO bond lengths. Here, the two spin coupling modes are of similar energies and geometries, and therefore only results of the ferromagnetically coupled modes were discussed in the Text. Another interesting feature for Cu is that after O_2 coordination, as illustrated in Figure 4, the His64 ligand moves out of the coordination sphere compared to the X-ray structure of Cu-Fe_BMb without O_2. Actually, in our initial setups for O_2 bound models, His64 is like at the X-ray structure used, i.e. it is coordinated with Cu, but the geometry optimization always end with it leaving the coordination sphere. In comparison, the geometry optimization of the X-ray structure without O_2 yields a structure with His64 still coordinated. These results suggest that in the biosynthetic model Cu-Fe_BMb, the binding of O_2 kicks off His64. A further analysis of the geometric parameters around this Cu center shows that, after His64 moves of the coordinate sphere, the Cu center is basically square planar. The four ligand set is a typical

coordination structure seen with Cu^{II}, and the HCO model[18] reported previously. These results further support the current results for Cu-Fe_BMb-O_2.

Supplementary tables and figures:

Supplementary table S1| UV-Vis spectral features of Fe_BMb and WTMb

	ferric*			deoxy*	
	Soret	vis		Soret	vis
Fe_BMb	406	501	630	432	556
WTMb	408	502	628	429	556

*wavelength maxima reported (in nm)

Supplementary table S2| Key parameters of optimized models

Model	ρ_{Fe} (e)	ρ_{M} (e)	ρ_{O2} (e)	R_{OO} (Å)	R_{FeO} (Å)	R_{MO} (Å)	R_{FeM} (Å)	∠FeOO (degree)	∠MOO (degree)	Q_{O2} (e)*
E-Fe$_B$Mb-O$_2$	1.222	N/A	-0.375	1.277	1.869	N/A	N/A	119.5	N/A	-0.398
Zn-Fe$_B$Mb-O$_2$	1.061	0.001	-1.008	1.298	1.863	2.340	4.891	118.2	116.7	-0.528
Fe-Fe$_B$Mb-O$_2$-AF	-0.999	3.920	0.755	1.334	1.843	1.997	4.606	118.1	118.5	-0.699
Fe-Fe$_B$Mb-O$_2$-F	1.017	3.965	0.759	1.351	1.881	1.960	4.620	118.4	118.5	-0.773
Cu-Fe$_B$Mb-O$_2$-AF	-0.793	0.559	0.000	1.379	1.784	1.914	4.091	119.0	116.3	-0.883
Cu-Fe$_B$Mb-O$_2$-F	0.812	0.585	0.488	1.391	1.791	1.913	4.132	117.2	114.7	-0.917

*e is the charge corresponding to one electron

Supplementary table S3| Relative energies between anti-ferromagnetic and ferromagnetic spin coupling

Model	**ΔE** (kcal/mol)	**ΔE_{ZPE}** (kcal/mol)	**ΔH** (kcal/mol)	**ΔG** (kcal/mol)
Fe-Fe_BMb-O_2-AF	0.00	0.00	0.00	0.00
Fe-Fe_BMb-O_2-F	-0.27	-0.32	-0.48	-0.06
Cu-Fe_BMb-O_2-AF	0.00	0.00	0.00	0.00
Cu-Fe_BMb-O_2-F	1.78	1.47	1.64	-0.11

Supplementary table S4| Relative energies of different spin states for Fe-Fe$_B$Mb-O$_2$

Spin State	**ΔE** (kcal/mol)	**ΔE$_{ZPE}$** (kcal/mol)	**ΔH** (kcal/mol)	**ΔG** (kcal/mol)
Doublet	16.50	17.30	16.75	19.85
Quartet	5.19	4.90	5.20	4.84
Sextet	0.00	0.00	0.00	0.00

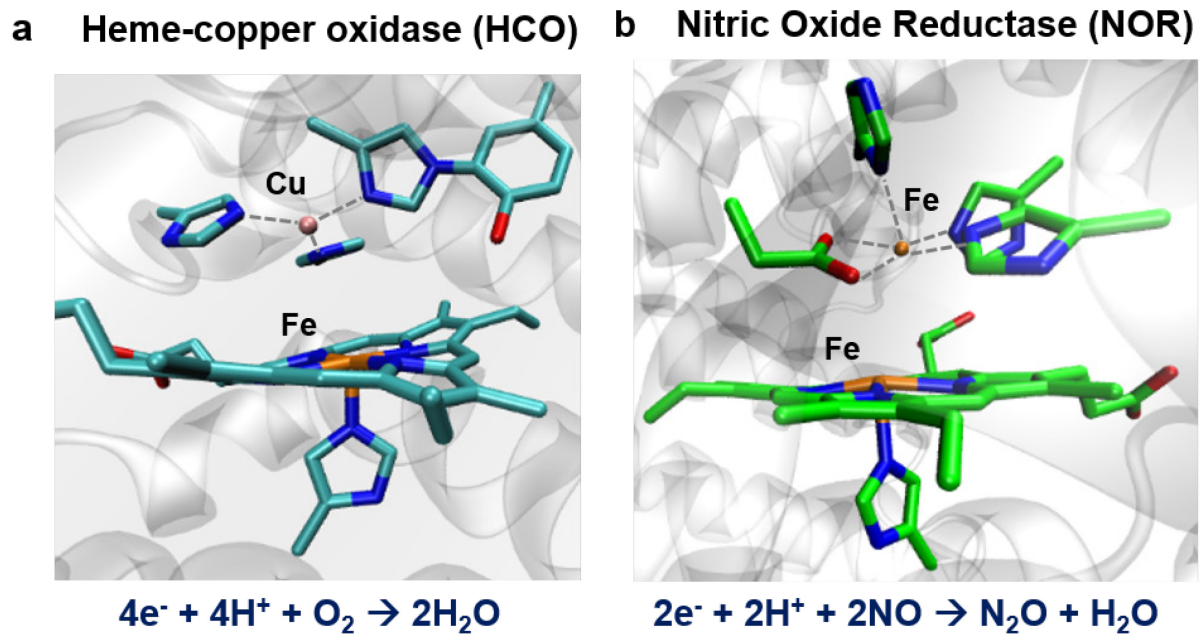

Supplementary figure S1| Structure of catalytic center of native HCO and NOR (a) The heterobinuclear heme-copper catalytic center of *cbb*$_3$ oxidase from P. stutzeri (PDB: 3MK7) (b) The heterobinuclear heme-nonheme iron catalytic center of *c*NOR from P. aeruginosa (PDB: 3O0R). The heme and amino acid residues as shown in licorice while the nonheme metal ions are shown in VDW representation as a sphere.

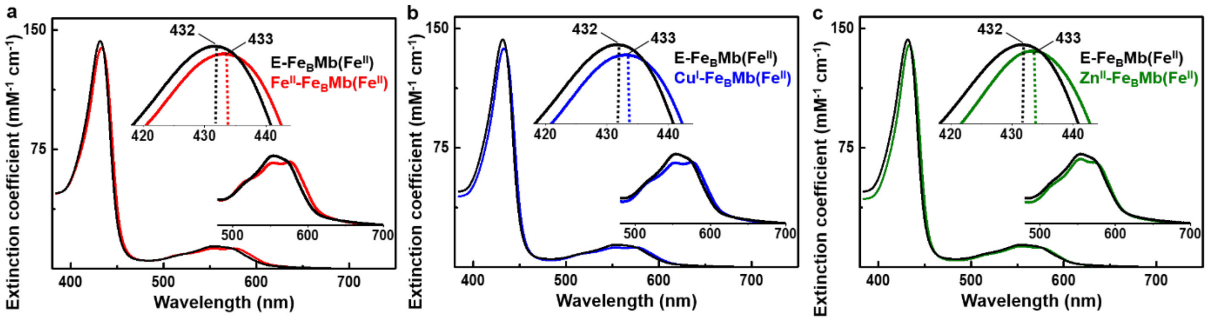

Supplementary figure S2| UV-Vis spectra of Fe_BMb variants. The UV-Vis spectra of the E-Fe_BMb(Fe^{II}) in black and Fe^{II}-added (A), Cu^{I}-added (B) and Zn^{II}-added Fe_BMb(Fe^{II}) in red, blue and green respectively.

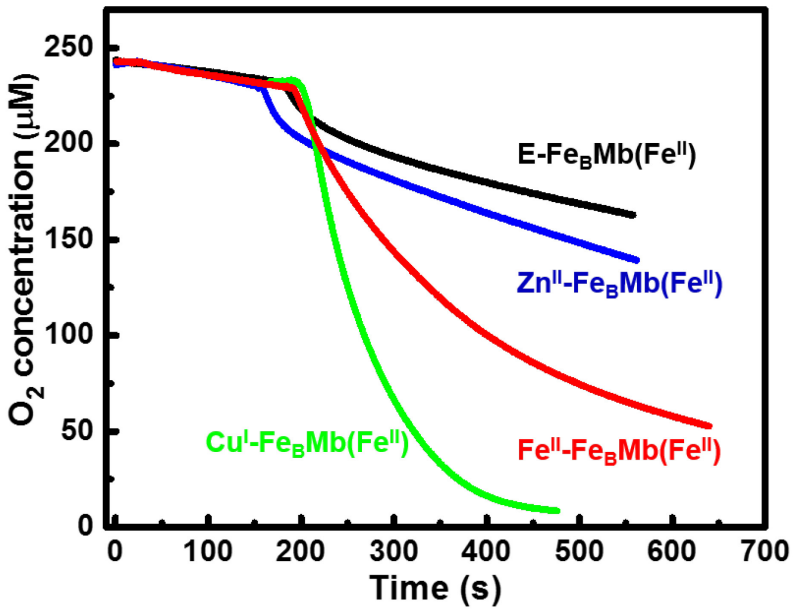

Supplementary figure S3| Oxygen consumption by different Fe$_B$Mb variants. The results of the oxygen reduction enzymatic assay performed on the oxygen electrode. The experiments were performed on 18 μM Fe$_B$Mb variants in 100 mM phosphate buffer (pH 6) containing ~250 μM O_2, 1.8 mM TMPD, and 18 mM ascorbate.

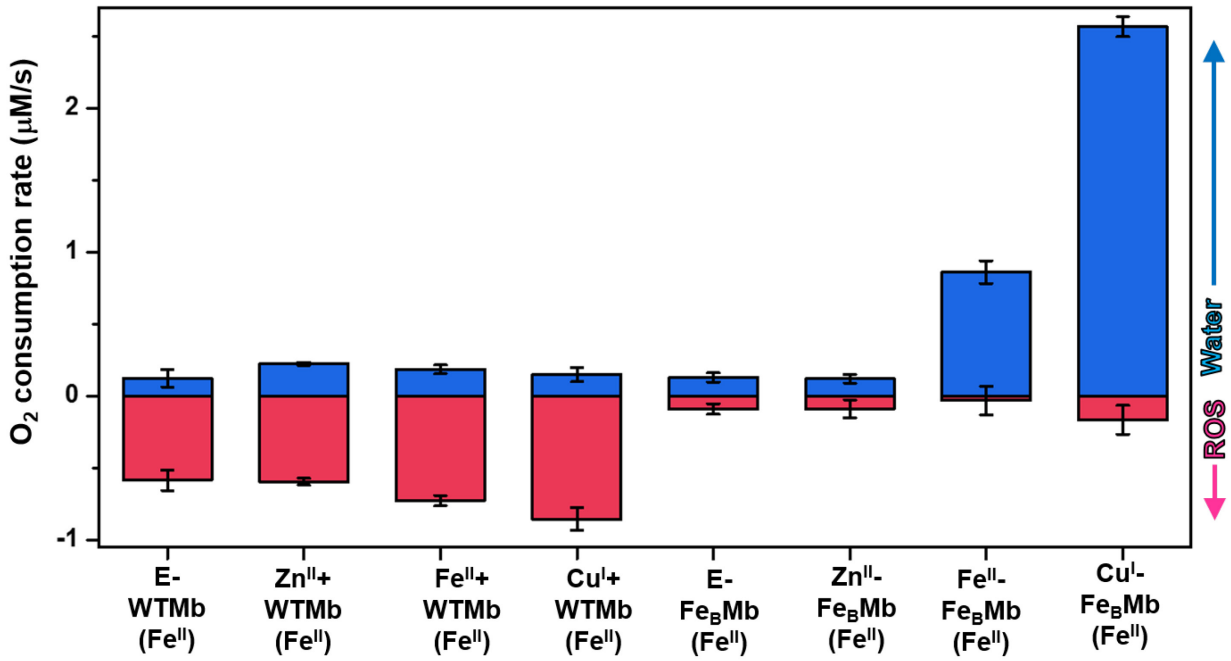

Supplementary figure S4| Oxidase activity of Fe_BMb variants and metal-added WTMb. The rates of oxygen reduction to form either H_2O (blue) or ROS (red) catalyzed by 18 μM Fe_BMb variants in 100 mM phosphate buffer (pH 6) containing ~250 μM O_2, 1.8 mM TMPD, and 18 mM ascorbate. Error bars indicate standard deviation.

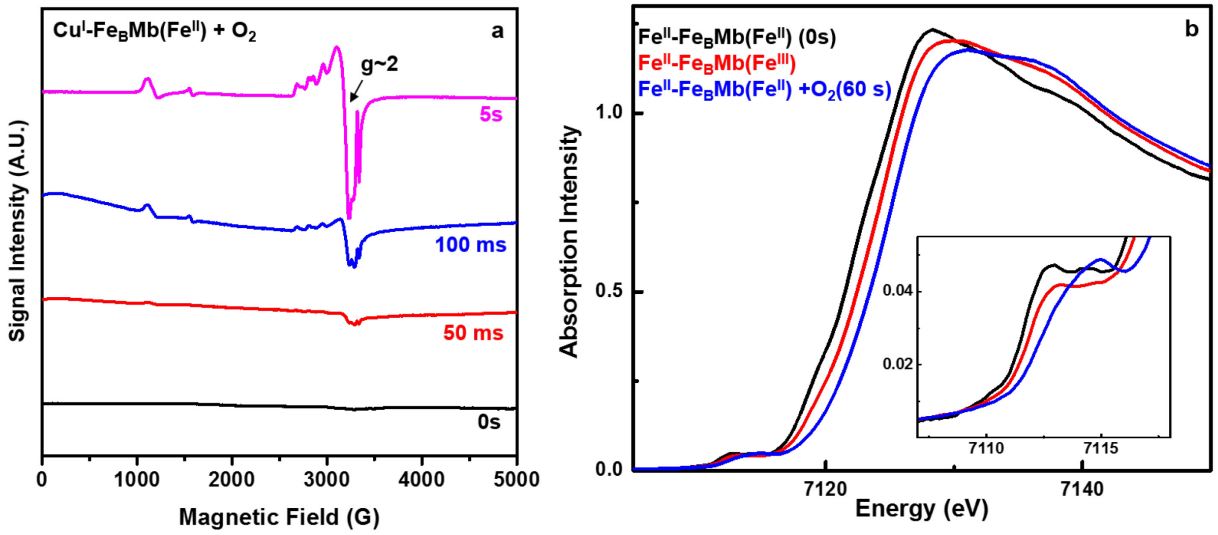

Supplementary figure S5 | Oxidation of Cu^{I} and Fe^{II} at the nonheme center on reaction with oxygen. (a) The reaction of Cu^{I}-Fe$_B$Mb(Fe^{II}) with oxygen as probed by EPR spectroscopy. Cu^{I}-Fe$_B$Mb(Fe^{II}) (0.2 mM) was reacted with O_2 (0.9 mM) and quenched at different time points as indicated. The EPR spectra was collected at 30K, 5 mW power, and 9.05 GHz. The continuous increase in the four-line anisotropic signal at g~2 indicates the oxidation of Cu^{I} to Cu^{II} by donation of an electron to the oxygen substrate. (b) The reaction of Fe^{II}-Fe$_B$Mb(Fe^{II}) with oxygen as probed by XANES spectroscopy. Fe^{II}-Fe$_B$Mb(Fe^{II}) (1.6 mM) was reacted with excess O_2 and quenched at 0s and 60s. Additionally, a control sample of Fe^{II}-Fe$_B$Mb(Fe^{III}) (1.4 mM) was also prepared. The XANES spectra show a typical decrease in absorption intensity as well as a 3-4 eV increase in edge energy consistent with oxidation of iron. The increase in edge energy for diferrous Fe^{II}-Fe$_B$Mb(Fe^{II}) samples from 7118.5 eV (black) to 7125.1 eV (blue) on reaction with oxygen indicates the oxidation of Fe^{II} to Fe^{III}. The control "semi-met" spectrum (red) exhibits an intermediate edge energy of 7122.2 eV, indicating that the nonheme Fe^{II} is oxidized to Fe^{III} on reaction with oxygen. Inset shows the pre-edge features of the XANES spectra where the diferrous spectrum shows a nearly symmetrical split peak (first transition 7112.8eV) that becomes less distinct for the semi-met sample (7113.1eV). The diferric 60s sample pre-edge peak (7114.9eV) is asymmetric, suggesting an oxo-bridging ligand between the two Fe atoms.

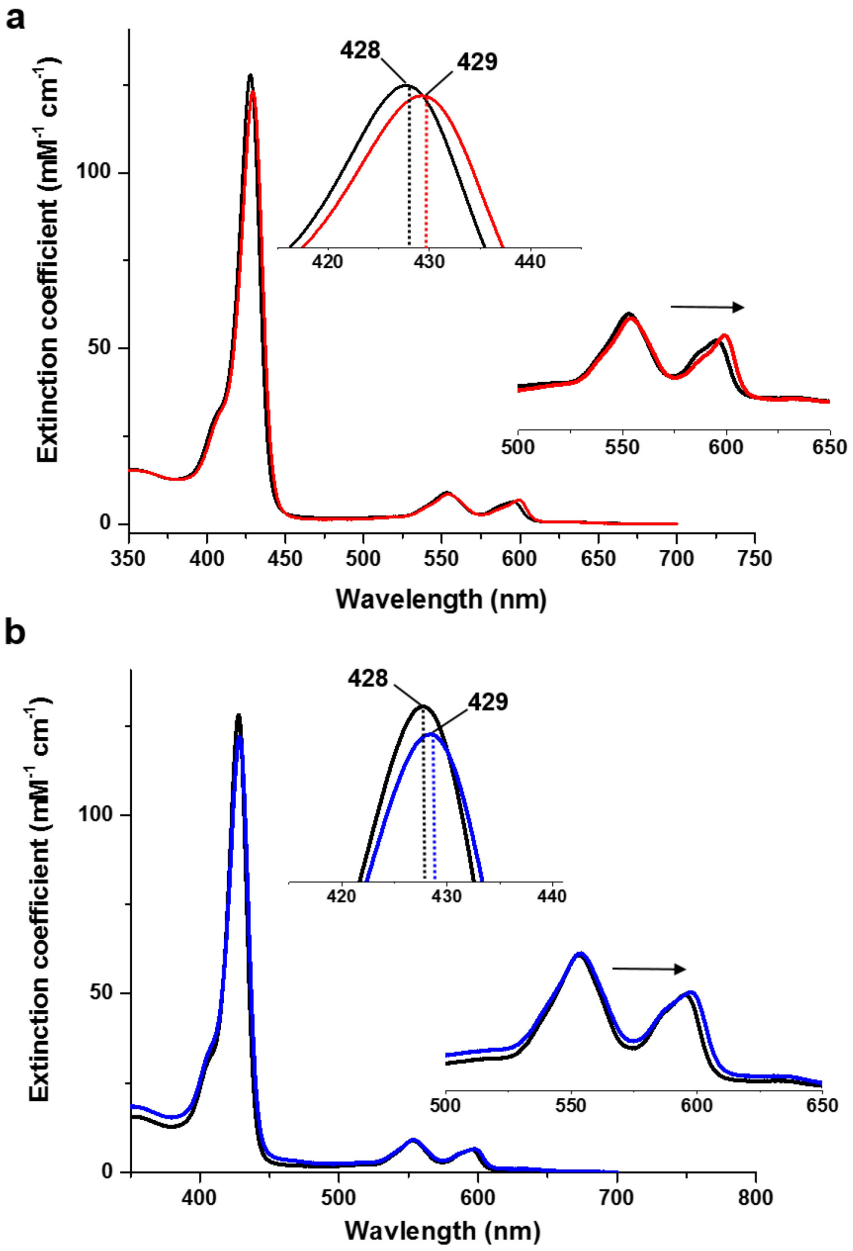

Supplementary figure S6| UV-Vis spectra of nonheme metal-added $Fe_BMb(Zn^{II})$ variants (A) The UV-Vis spectrum of E-(in black) and Fe^{II}-$Fe_BMb(Zn^{II})$ (in red). (B) The UV-Vis spectrum of E-(in black) and Cu^{I}-$Fe_BMb(Zn^{II})$ (in blue).

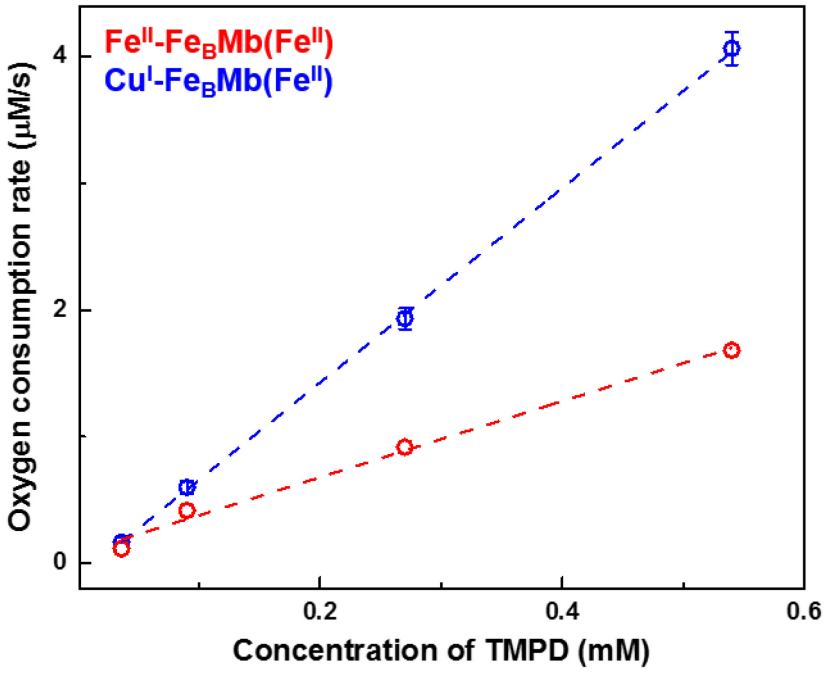

Supplementary figure S7| Oxygen reduction activity of Fe$_B$Mb variants with increasing electron donor concentration. Oxygen reduction reactivity of Fe^{II}- and Cu^{I}-Fe$_B$Mb(Fe^{II}) with increasing TMPD/ascorbate concentration. The reaction was carried out by 6 μM Fe$_B$Mb variants in 100 mM phosphate buffer (pH 6) containing ~0.25 mM O_2 and varying TMPD/ascorbate concentrations. The ascorbate was kept at 1000 eq. of TMPD. Error bars indicate standard deviation.

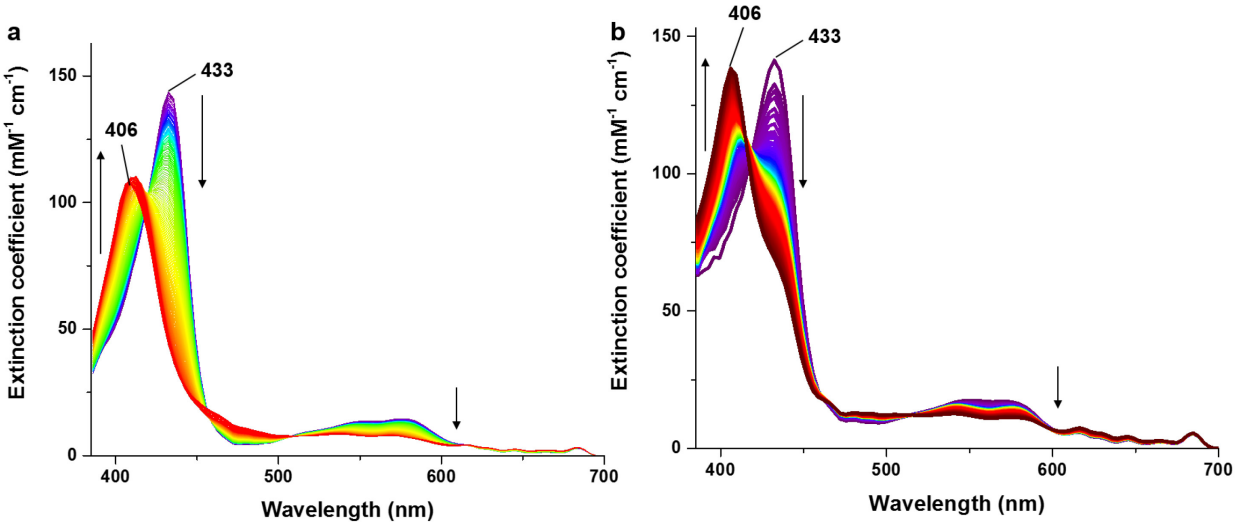

Supplementary figure S8| Stopped-flow UV-Vis measurement of the reaction between oxygen and Fe^{II}-/Cu^{I}-$Fe_BMb(Fe^{II})$. The stopped-flow UV-Vis measurements of the reaction between 10 μM of Fe^{II}-$Fe_BMb(Fe^{II})$ (a) and 10 μM of Cu^{I}-$Fe_BMb(Fe^{II})$ (B) and oxygen saturated buffer between 0.001s to 30s. Both the reactions showed a loss of $heme Fe^{II}$ species (in purple) and a gain in $heme Fe^{III}$ species (in red). No clean heme-oxy species was shown indicating rapid reaction of any bound oxygen with nearby redox active metal.

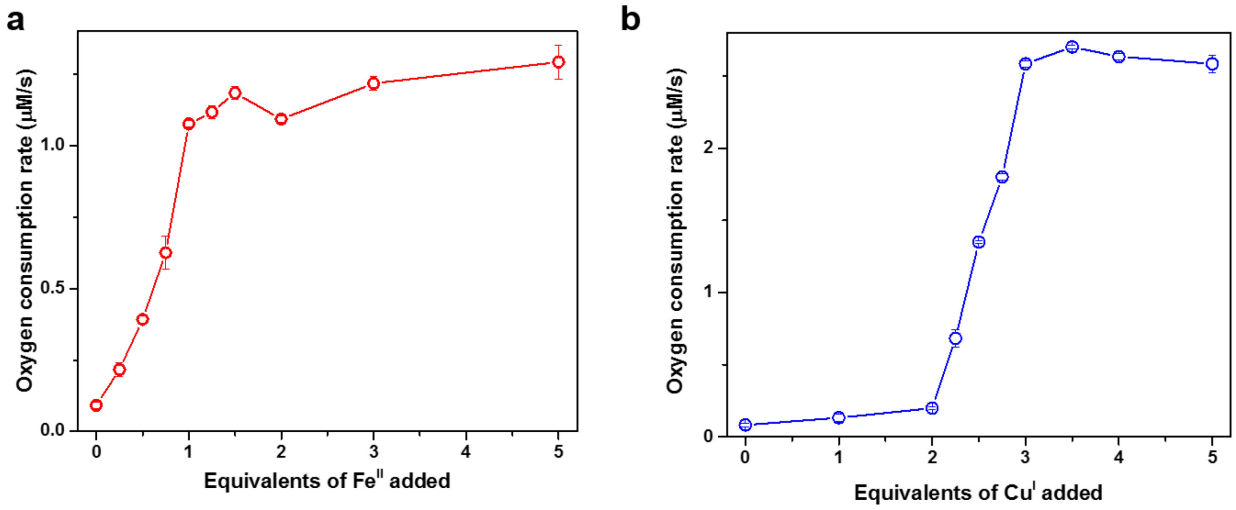

Supplementary figure S9| Oxygen reduction rates of Fe_BMb with increasing equivalents of Fe^{II} and Cu^{I} added. The experiments were conducted with designated equivalent of nonheme metal-added 18 μM $Fe_BMb(Fe^{II})$ in 100 mM phosphate buffer (pH 6) containing ~250 μM O_2, 1.8 mM TMPD, and 18 mM ascorbate. Error bars indicate standard deviation.

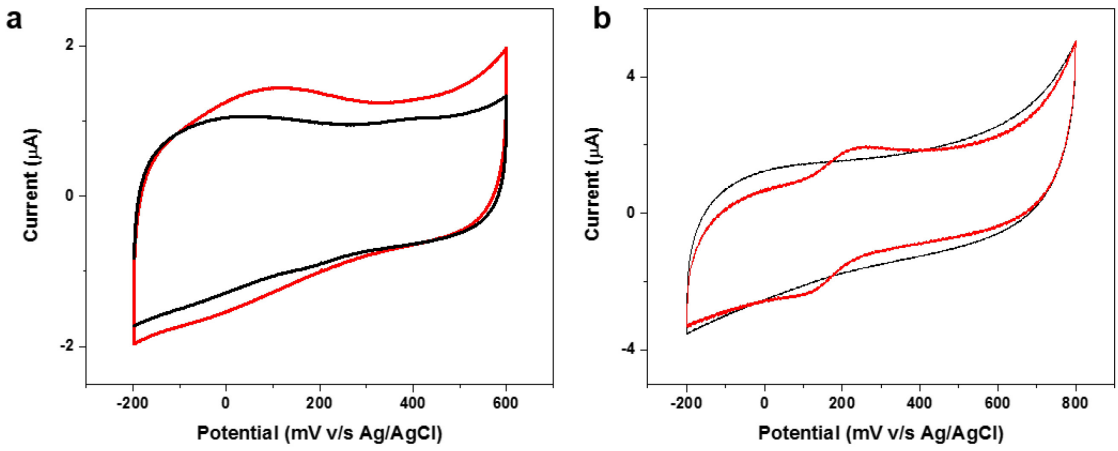

Supplementary figure S10| CV studies on Fe^{II}- and Cu^{I}-added $Fe_BMb(Zn^{II})$ variants. The CV data obtained for Fe^{II}- (A) and Cu^{I}- added $Fe_BMb(Zn^{II})$ (B). The red trace is for the protein while the black trace is that of blank electrode.

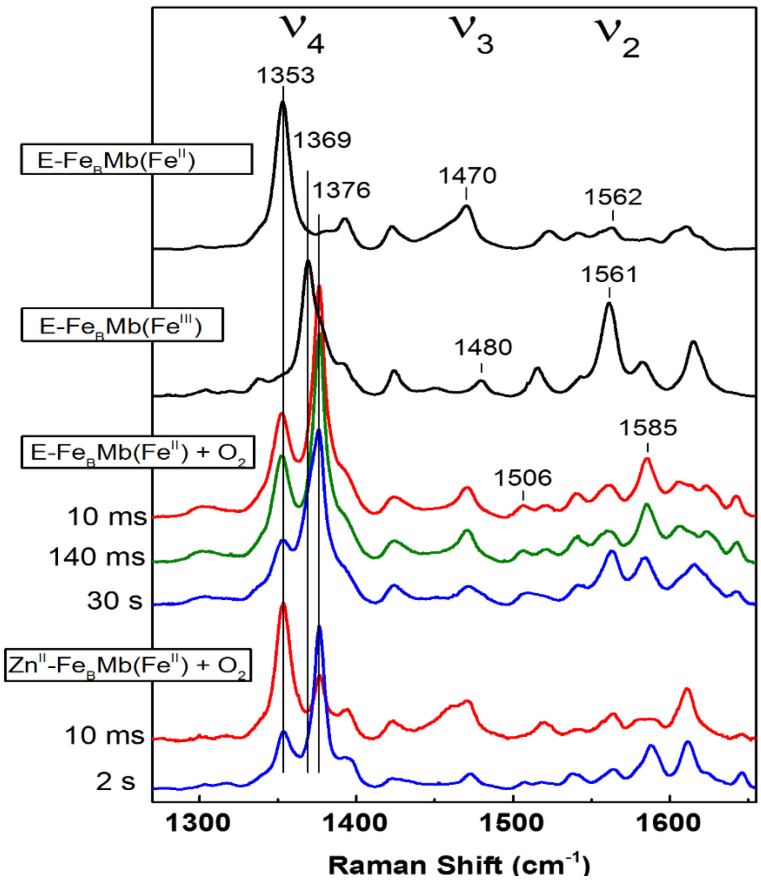

Supplementary figure S11| High-frequency RR spectra. Comparison of the RR spectra (110 K) of E-Fe$_B$Mb(Fe^{II}) and E-Fe$_B$Mb(Fe^{III}) (top black traces) with representative spectra of rapid-freeze-quench samples of the reaction of E-Fe$_B$Mb(Fe^{II}) and Zn^{II}-Fe$_B$Mb(Fe^{II}) with O_2 (color traces).

Supplementary references:

1 Miner, K. D. *et al.* A designed functional metalloenzyme that reduces O_2 to H_2O with over one thousand turnovers. *Angew. Chem. Intl. Ed.* **51**, 5589-92 (2012).

2 Sigman, J. A., Kim, H. K., Zhao, X. A., Carey, J. R. & Lu, Y. The role of copper and protons in heme-copper oxidases: Kinetic study of an engineered heme-copper center in myoglobin. *Proc. Natl. Acad. Sci. U. S. A.* **100**, 3629-34 (2003).

3 Sigman, J. A., Kwok, B. C. & Lu, Y. From myoglobin to heme-copper oxidase: Design and engineering of a Cu_B center into sperm whale myoglobin. *J. Am. Chem. Soc.* **122**, 8192-96 (2000).

4 Bhagi-Damodaran, A., Petrik, I. D., Marshall, N. M., Robinson, H. & Lu, Y. Systematic tuning of heme redox potentials and its effects on O_2 reduction rates in a designed oxidase in myoglobin. *J. Am. Chem. Soc.* **136**, 11882-85 (2014).

5 Brunori, M., Saggese, U., Rotilio, G. C., Antonini, E. & Wyman, J. Redox equilibrium of sperm-whale myoglobin, aplysia myoglobin, and *chironomus thummi* hemoglobin. *Biochemistry* **10**, 1604-& (1971).

6 Lin, Y.-W. *et al.* Roles of glutamates and metal ions in a rationally designed nitric oxide reductase based on myoglobin. *Proc. Natl. Acad. Sci. U. S. A.* **107**, 8581-6 (2010).

7 Liu, X. *et al.* Significant increase of oxidase activity through the genetic incorporation of a tyrosine-histidine cross-link in a myoglobin model of heme-copper oxidase. *Angew. Chem. Intl. Ed.* **51**, 4312-6 (2012).

8 Chakraborty, S. *et al.* Spectroscopic and computational study of a nonheme iron nitrosyl center in a biosynthetic model of nitric oxide reductase. *Angew. Chem. Intl. Ed.* **126**, 2449-53 (2014).

9 Matsumura, H. & Moenne-Loccoz, P. Characterizing millisecond intermediates in hemoproteins using rapid-freeze-quench resonance raman spectroscopy. *Methods Mol. Biol.* **1122**, 107-23 (2014).

10 Ling, Y. & Zhang, Y. Moessbauer, nmr, geometric, and electronic properties in S = 3/2 iron porphyrins. *J. Am. Chem. Soc.* **131**, 6386-88 (2009).

11 Zhang, Y. & Oldfield, E. On the mossbauer spectra of isopenicillin n synthase and a model {FeNO}7 (s = 3/2) system. *J. Am. Chem. Soc.* **126**, 9494-95 (2004).

12 Zhang, Y. & Oldfield, E. NMR hyperfine shifts in blue copper proteins: A quantum chemical investigation. *J. Am. Chem. Soc.* **130**, 3814-23 (2008).

13 Yang, L., Ling, Y. & Zhang, Y. HNO binding in a heme protein: Structures, spectroscopic properties, and stabilities. *J. Am. Chem. Soc.* **133**, 13814-17 (2011).

14 Chen, H., Ikeda-Saito, M. & Shaik, S. Nature of the Fe-O_2 bonding in oxy-myoglobin: Effect of the protein. *J. Am. Chem. Soc.* **130**, 14778-90 (2008).

15 Frisch, M. J. T., G. W.; Schlegel, H. B.; Scuseria, G. E.; Robb, M. A.; Cheeseman, J. R.; Scalmani, G.; Barone, V.; Mennucci, B.; Petersson, G. A.; Nakatsuji, H.; Caricato, M.; Li, X.; Hratchian, H. P.; Izmaylov, A. F.; Bloino, J.; Zheng, G.; Sonnenberg, J. L.; Hada, M.; Ehara, M.; Toyota, K.; Fukuda, R.; Hasegawa, J.; Ishida, M.; Nakajima, T.; Honda, Y.; Kitao, O.; Nakai, H.; Vreven, T.; Montgomery, Jr., J. A.; J. Peralta, E.; Ogliaro, F.; Bearpark, M.; Heyd, J. J.; Brothers, E.; Kudin, K. N.; Staroverov, V. N.; Keith, T.; Kobayashi, R.; Normand,J.; Raghavachari, K.; Rendell, A.; Burant, J. C.; Iyengar, S. S.; Tomasi, J.; Cossi, M.; Rega, N.; Millam, J. M.; Klene, M.; Knox, J. E.; Cross, J. B.; Bakken, V.; Adamo, C.; Jaramillo, J.; Gomperts, R.; Stratmann, R. E.; Yazyev, O.; Austin, A. J.; Cammi, R.; Pomelli, C.; Ochterski, J. W.; Martin, R. L.; Morokuma, K.;

Zakrzewski,V. G.; Voth, G. A.; Salvador, P.; Dannenberg, J. J.; Dapprich, S.; Daniels, A. D.; Farkas, O.; Foresman, J. B.; Ortiz, J. V.; Cioslowski, J.; Fox, D. J. Gaussian 09, revision d.01. *Gaussian, Inc.: Wallingford CT* (2013).

16 Zhang, Y., Mao, J., Godbout, N. & Oldfield, E. Mossbauer quadrupole splittings and electronic structure in heme proteins and model systems: A density functional theory investigation. *J. Am. Chem. Soc.* **124**, 13921-30 (2002).

17 Michael, M. A. *et al.* HNO/NO conversion mechanisms of Cu-based HNO probes with implications for Cu,Zn-SOD. *J. Phys. Chem. Lett.* **5**, 1022-26 (2014).

18 Noodleman, L., Han Du, W.-G., Fee, J. A., Gotz, A. W. & Walker, R. C. Linking chemical electron-proton transfer to proton pumping in cytochrome c oxidase: Broken-symmetry DFT exploration of intermediates along the catalytic reaction pathway of the iron-copper dinuclear complex. *Inorg. Chem.* **53**, 6458-72 (2014).